

# FEASIBILITY ANALYSIS OF THE WING BOX STRUCTURE FOR THE RAYMER MANNED MARS AIRPLANE

14 April 2021, Leganes, Madrid, Spain

Arturo Gómez

Department of Continuum Mechanics and Structural Analysis. University Carlos III of Madrid.  
Avda. de la Universidad 30, 28911 Leganés, Madrid, Spain

Telephone number: +34 674997308

Email address: edgomez@ing.uc3m.es

ORCID A. Gómez: <http://orcid.org/0000-0002-1762-9396>

## Introduction

This manuscript describes the feasibility analysis of the wing box structure of the Raymer Manned Mars Airplane concept (Dash-2 version) configured for exploration, research, cargo transport, photography, and the linking of multiple settlements [1]. This analysis covers a preliminary loading estimation analysis of critical symmetric flight manoeuvres, a preliminary wing architecture design, and a full-scale structural static and buckling analysis using Finite Element Analysis. Results show that the proposed wing box architecture is able to support the limit loads without failure or permanent deformation and that the deformation is maintained within the limits for safe operation.

*Disclaimer: This study was carried out as part of a design effort made by an international team of volunteers for the AIAA 2021 SciTech Forum in a record period of one month. Design reviews were limited and multiple assumptions had to be made in the process. For this reason, the content of this manuscript must be taken with caution.*

## Nomenclature

AFT	Afterward
b	Wing's span
$E_1, E_2$	Young's modulus in the longitudinal and transverse direction
FWD	Forward
$G_{12}$	Shear modulus
n	Load factor
L	Lift force

MTOW	Maximum take-off weight
T	Trust force
$V_a$	Manouvering speed
$V_D$	Dive speed
$X^T$	Longitudinal tensile strength
$X^C$	Longitudinal compressive strength
y	Wing station position
$Y^T$	Transverse tensile strength
$Y^C$	Transverse compressive strength
$S^L$	Longitudinal shear strength
$S^T$	Transverse shear strength
$F_f^t, F_f^c, F_m^t, F_m^c$	Hashin's failure indexes
$\sigma_{ij}$	Stress tensor components
$\lambda_n$	nth eigenvalue

### Requirements

The integrity of the structure is assessed by complying with the following Airworthiness Standards applicable to sailplanes:

#### CS 22.301 Loads

- (a) Strength requirements are specified in terms of limit loads (the maximum loads to be expected in service) and ultimate loads (limit loads multiplied by prescribed factors of safety). Unless otherwise provided, prescribed loads are limit loads.
- (b) Unless otherwise provided, the air and ground loads must be placed in equilibrium with inertia forces, considering each item of mass in the sailplane. These loads must be distributed to represent actual conditions or a conservative approximation to them.

#### CS 22.303 Factor of safety

Unless otherwise provided, a factor of safety of 1.5 must be used

#### CS 22.305 Strength and deformation

- (a) The structure must be able to support limit loads without permanent deformation. At any load up to limit loads, the deformation may not interfere with safe operation. This applies in particular to the control system.

## 1. Loading estimations

Due to the limited scope of the current work, only quasi-static symmetrical positive and negative manoeuvres were analysed particularly those corresponding to the corners in the V-n diagram. Additionally, one condition of quasi-static take-off was analysed.

### 1.1. V-n diagram

A preliminary flight envelope was produced to determine the magnitude of critical loading conditions for symmetrical manoeuvres and gust conditions. The geometrical parameters and operating conditions used in this v-n diagram are shown in the table below.

The maximum loading factor is limited to 2.5 and -0.8 considering stiffness constraints due to the large wingspan of the aircraft. Those load factors are well below conventional values for conventional sailplanes (+5.3 and -2.6).

Due to the unavailability of detailed aerodynamic data at this stage, some assumptions were carried out based on similar category aeroplanes. Those assumptions are highlighted:

<b>INPUT</b>		
$\rho$ (Kg/m <sup>3</sup> )	0.020	Atmosphere density
$g$ (m/s <sup>2</sup> )	3.71	gravity acceleration
MTOW (Kg)	2721.6	Maximum take-off weight
$S$ (m <sup>2</sup> )	193.2	Wing area
MAC (m)	2.8	Mean aerodynamic chord
$n_1$ (g)	<b>2.5</b>	Max. Positive normal acceleration
$n_3$ (g)	<b>-0.8</b>	Max negative normal acceleration
$V_c$ (m/s)	<b>77.2</b>	Design cruise speed
$V_D$ (m/s)	<b>150</b>	Design dive speed
$dCL/d\alpha$ (per radian)	<b>4.967</b>	Airplane's lift curve slope
$CL_{max}$	<b>1.6</b>	Maximum lift coefficient
$CL_{min}$	<b>-0.8</b>	Minimum lift coefficient
$CD_{min}$	<b>0.01453</b>	Minimum drag coefficient
$\mu_g$	102.0	Longitudinal relative density
$F$	0.84	Alleviating factor
$CL_{Vc}$	0.88	
$\Delta ng_{Vc}$	0.9	
$CL_{V_D}$	0.2322	
$\Delta ng_{V_D}$	0.9	

Table 1. Parameters for V-n diagram

## 1.2. Gust Envelop

Wind speed in Mars varies from 2-7 m/s in summer to 5-10 m/s in autumn.

Every year there are moderate big dust storms on Mars that cover large areas (continent size) and can last for weeks. Additionally once every three years on Mars there are global dust storms. During such dust storms, the strongest wind can reach values around 17 to 30 m/s.

Dust is a big problem for the solar panels used to recharge the batteries of the aircraft. During a storm, dust can cover the solar panels by decreasing their efficiency. In the case of global dust storms, enough dust is thrown into the atmosphere reducing the sunlight reaching the surface of Mars.

Due to the low frequency of dust storms and the technical difficulties for the operation of the solar panels, it seems necessary to restrict the operation of the aircraft in such atmospheric conditions. Therefore, the gust conditions associated with dust storms are not analysed in the flight envelope.

The gust load factor is computed following the CS-22.341 standards for sailplanes and is given as:

$$n = 1 \pm \frac{\frac{k}{2} \rho U V_{\infty} a}{\frac{mg}{S}}$$

Where  $a$  is the slope of the wing lift curve slope and  $k$  is the gust alleviation factor given by the following formula:

$$k = \frac{0.88\mu}{5.3 + \mu}$$

Being the non-dimensional mass ratio:

$$\mu = \frac{\frac{2m}{S}}{\rho a(MAC)}$$

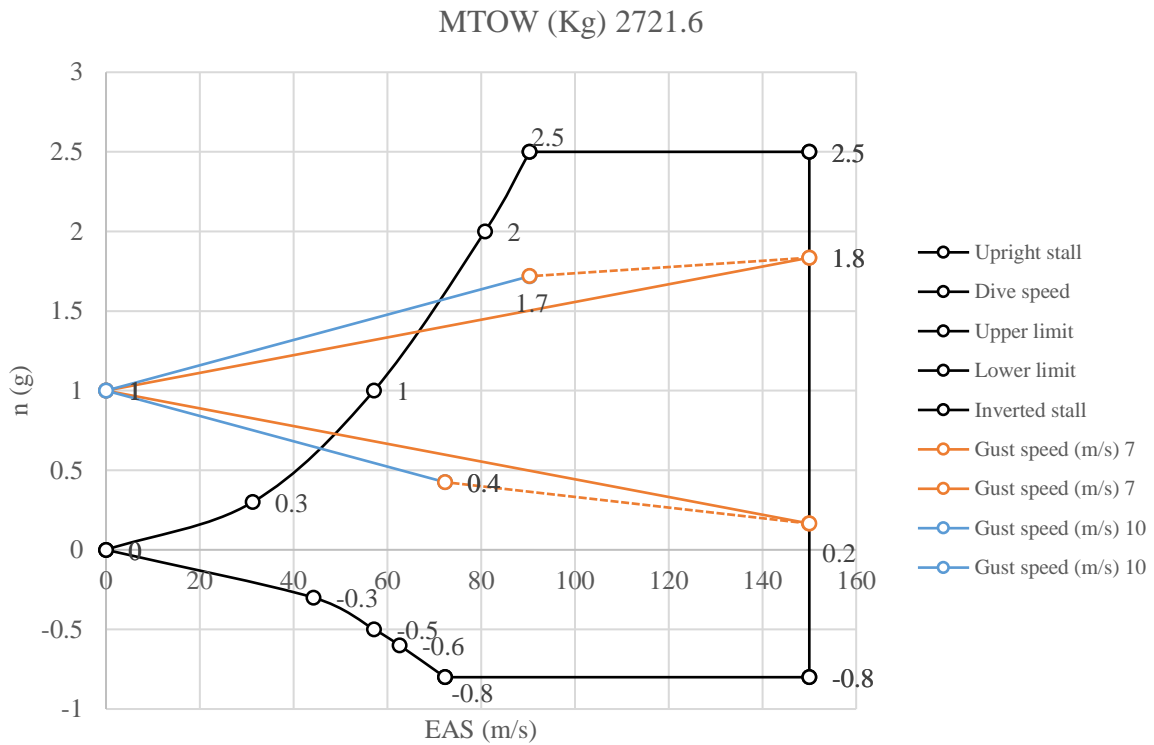


*Figure 1. V-n diagram*

### 1.3. Steady vertical take-off

During take-off, the aircraft is lifted vertically using 8 rockets located in the inboard nacelles.

Rocket trust (on earth - each):

$$T_i = 300 \text{ lbf} = 1334.47 \text{ N}$$

Total Trust (x8):

$$T = T_i(8) = 8(1334.47 \text{ N}) = 10675 \text{ N}$$

During the first seconds after take-off, the acceleration of the aircraft can be considered steady and the load factor is given by:

$$n_t = \frac{T}{mg} = \frac{10675 \text{ N}}{10093 \text{ N}} = 1.058$$

Due to the highly localized load and the inertia relief effects associated with the considerable span of the aircraft this loading condition seems to be critical.

The following are the loading cases to be analysed for sizing the wing structure.

Case	n (g)	Mass (Kg)	V (m/s)	Comment
0	1	2721	57.1	Steady level flight at $V_s$
I	2.5	2721	90.4	(+) symmetric at $V_a$
II	-0.8	2721	72.3	(-) symmetric at $V_a$
III	1.06	2721	N/A	Steady take-off with rockets (T= 10675 N)

#### 1.4. Mass distribution

The mass distribution along the spanwise is determined in order to include inertia relief in the analysis. Due to the lack of detailed information at this design stage some assumptions were made:

- The mass of the motor, motor installations, and controller and propeller are assumed in the location of the inboard and outboard nacelles.
- Rocket, rocket installations and are assumed to be located in the inboard nacelle.
- Batteries are located
- Solar cells are assumed to be located between 11.5m to 22.5m of the span.
- Batteries and batteries installations are assumed to be located in two locations at the following locations 4m to 5.5m (inboard) and 15m-16.5m (outboard).
- Equipment and crew ad payload assumed to be located in the centreline.

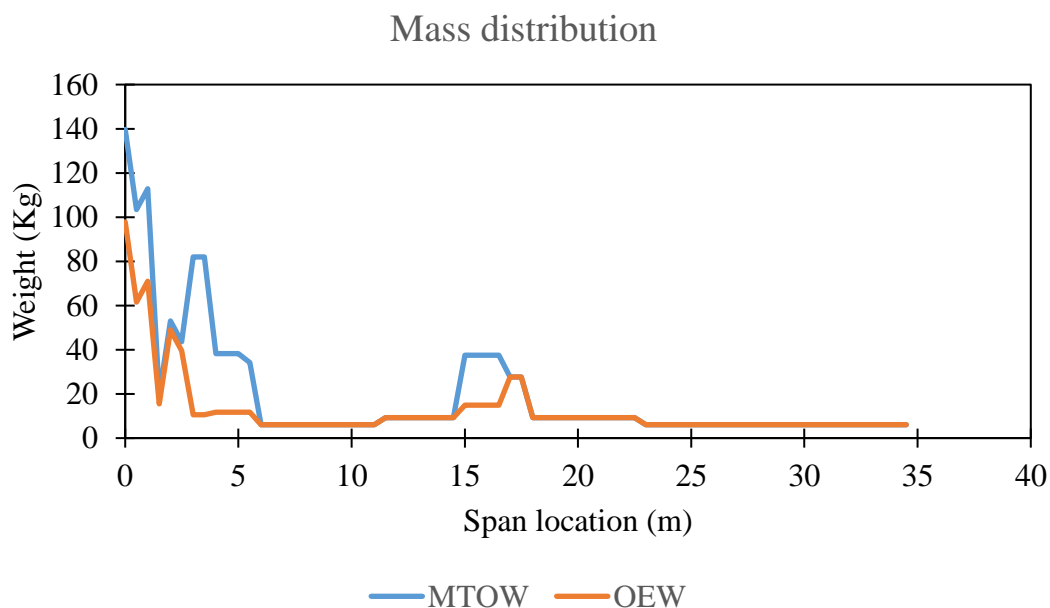


Figure 2. Span-wise mass distribution

## 1.5. Load diagrams

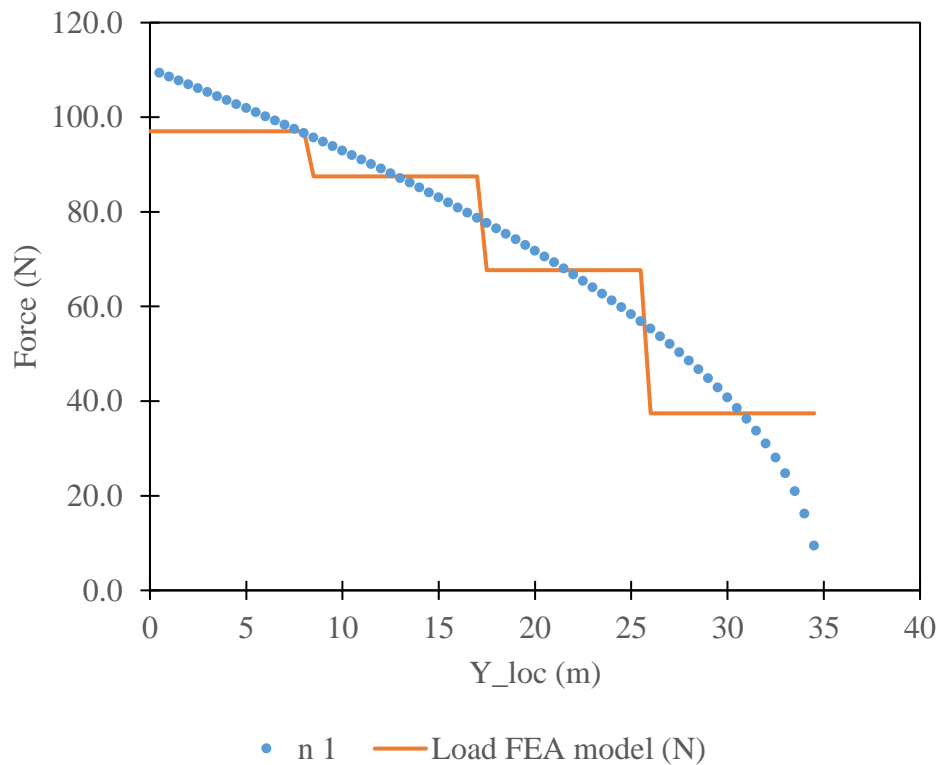
For loading estimation purposes, the lift distribution is assumed perfectly elliptical and given by the following equation [2]:

$$L'(y) = \rho V_{\infty} \Gamma_s \sqrt{1 - \left(\frac{y}{\frac{b}{2}}\right)^2}$$

Where the wing's lift coefficient is given by:

$$C_L = \frac{1}{\frac{1}{2} \rho V_{\infty} S} \int_{-b/2}^{+b/2} L'(y) dy$$

The lift coefficient is computed for each loading condition-based and the circulation at the root  $\Gamma_s$  is obtained by iteration. The following figures show the lift distribution for each analysed load case. To simplify the load pattern for the FEA analysis the exact lift distribution is approximated in four-step distributions.



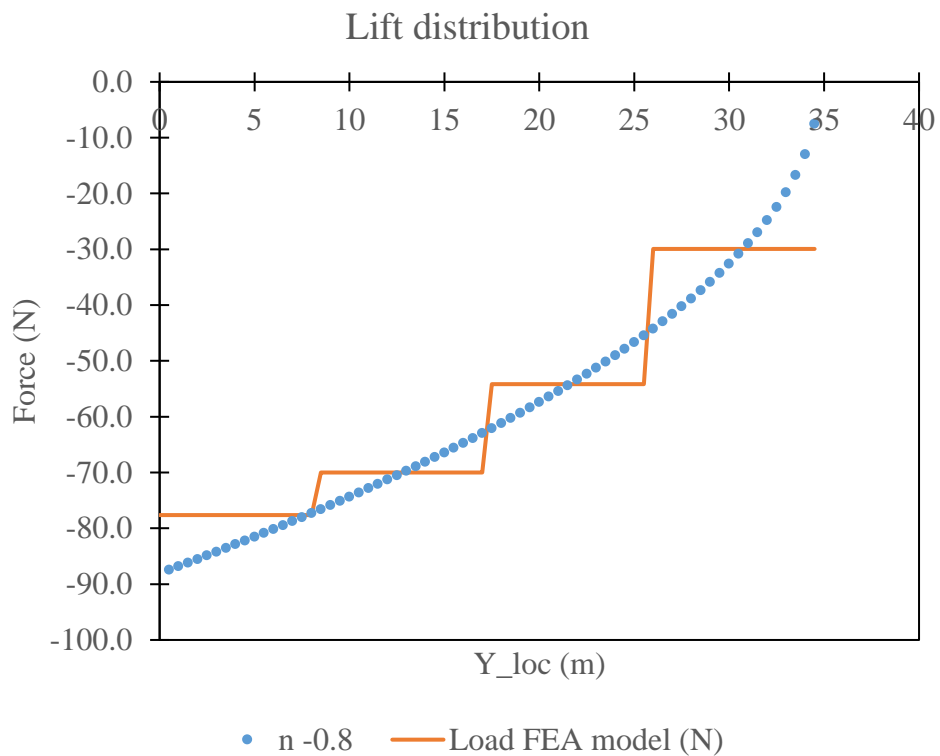
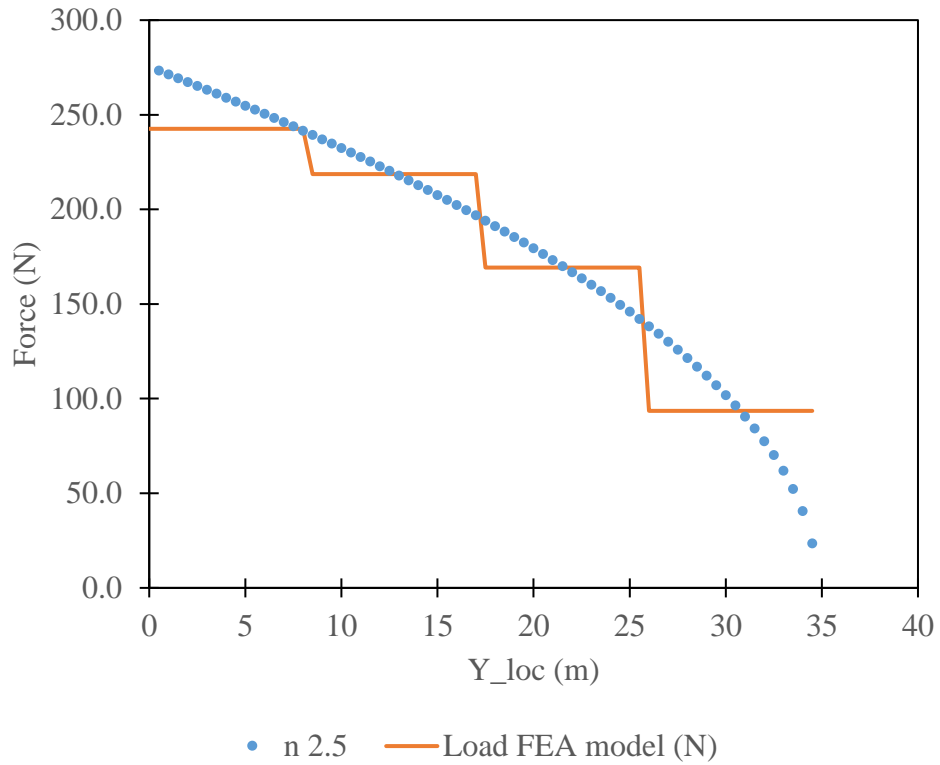


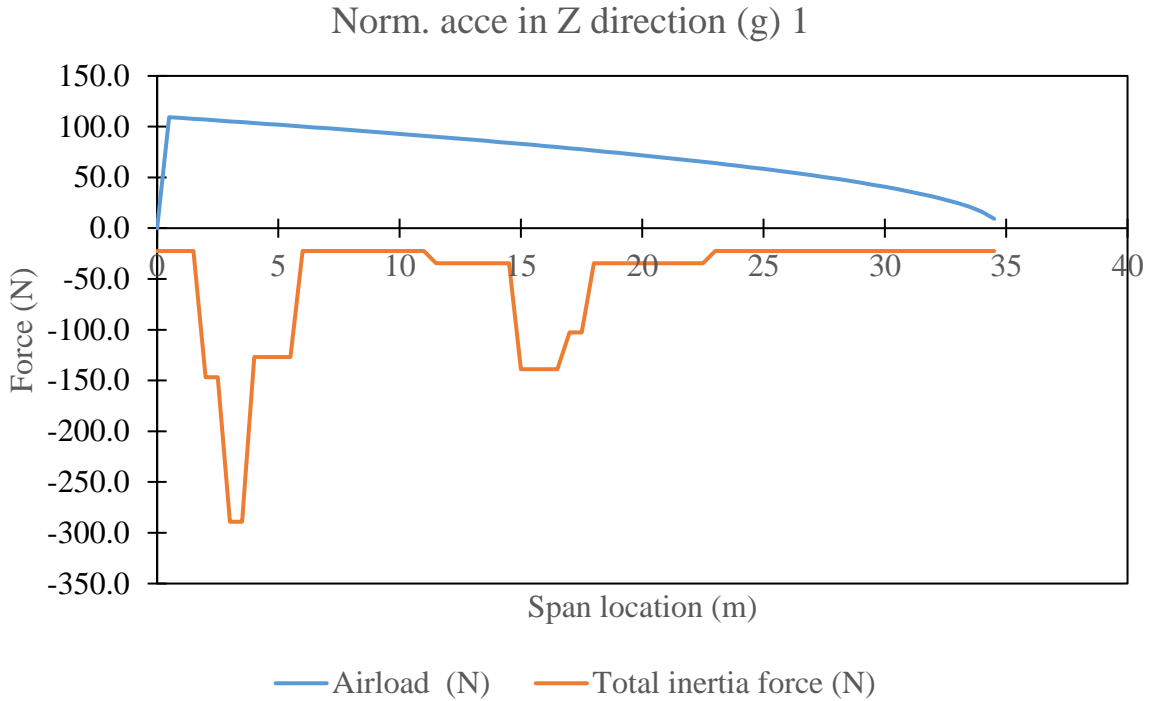
Figure 3. Span-wise lift distribution. a) Case 0 , b) Case I, c) Case II, d) Case III

The shear force and bending moment diagrams are computed at each wing station including the contributions from the aerodynamic lift distribution and inertial relief load at different span

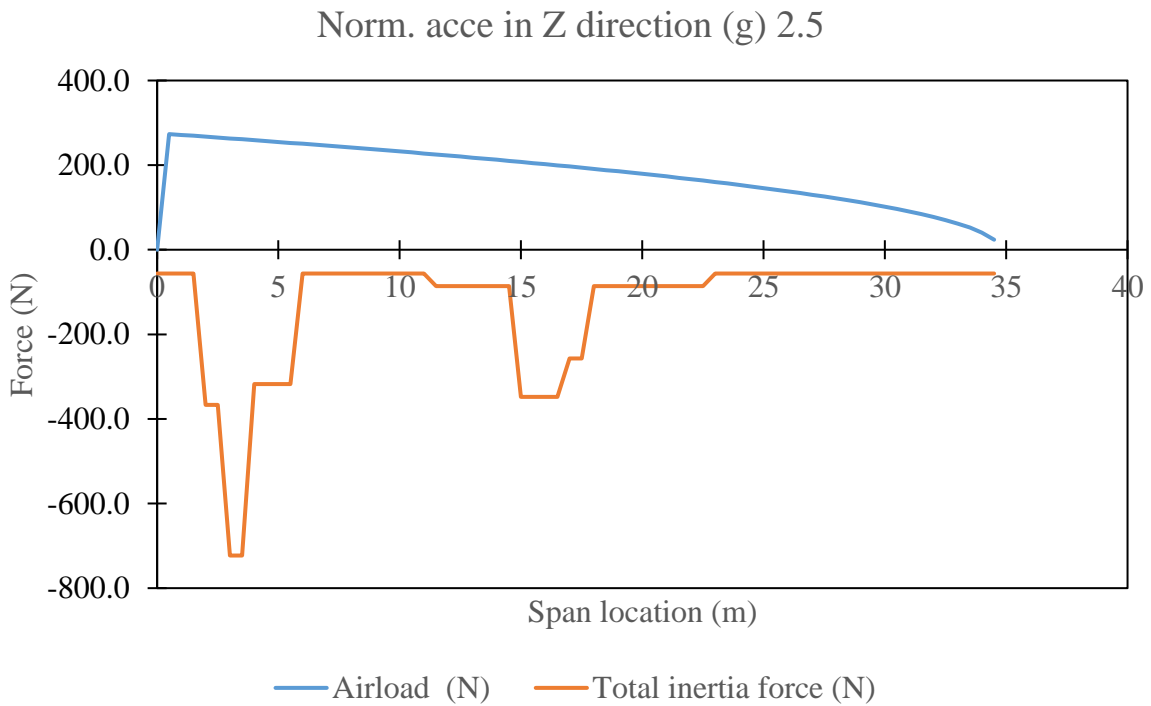


stations. This calculation method ensures that inertial load are placed in equilibrium with aerodynamics forces and moment. Further information about this method can be found in [3].

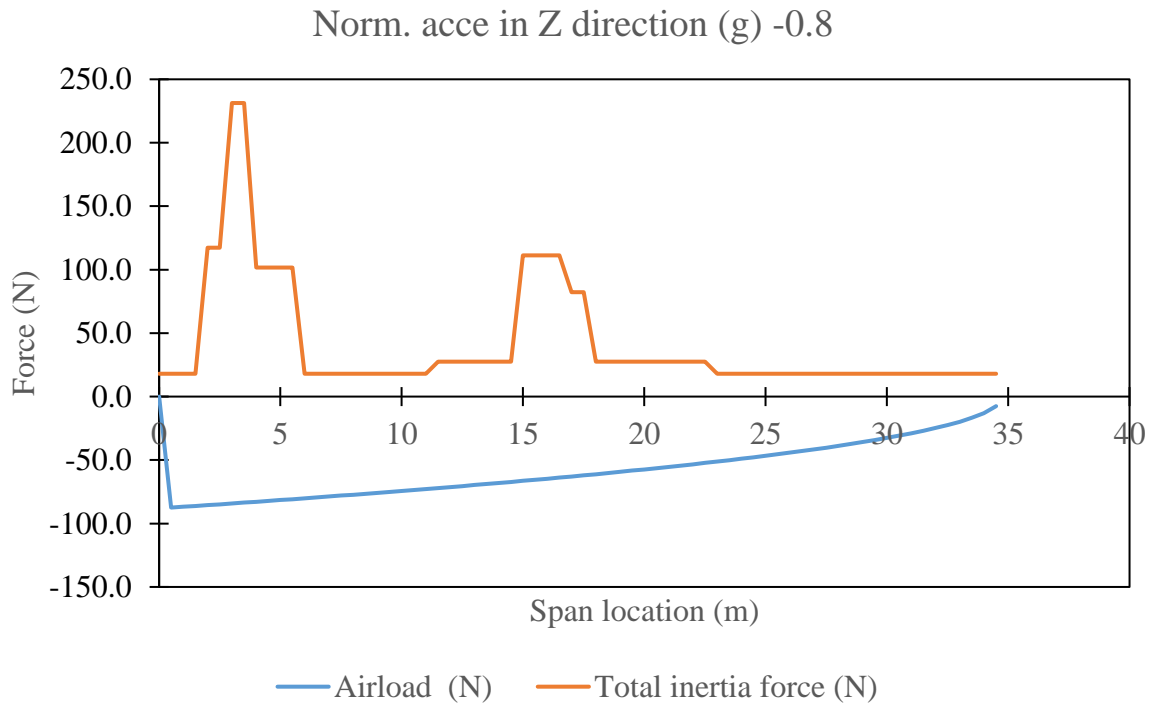
The load diagrams used for the estimation of the shear and moment diagrams are summarized as follows.



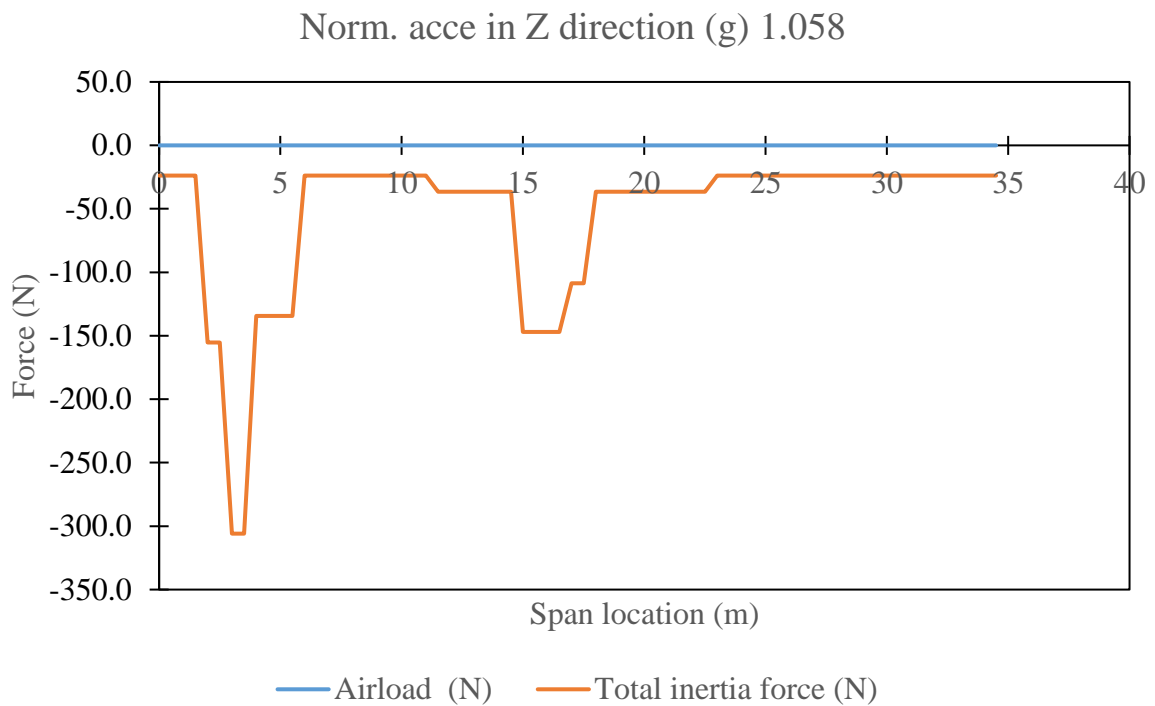
a)



b)

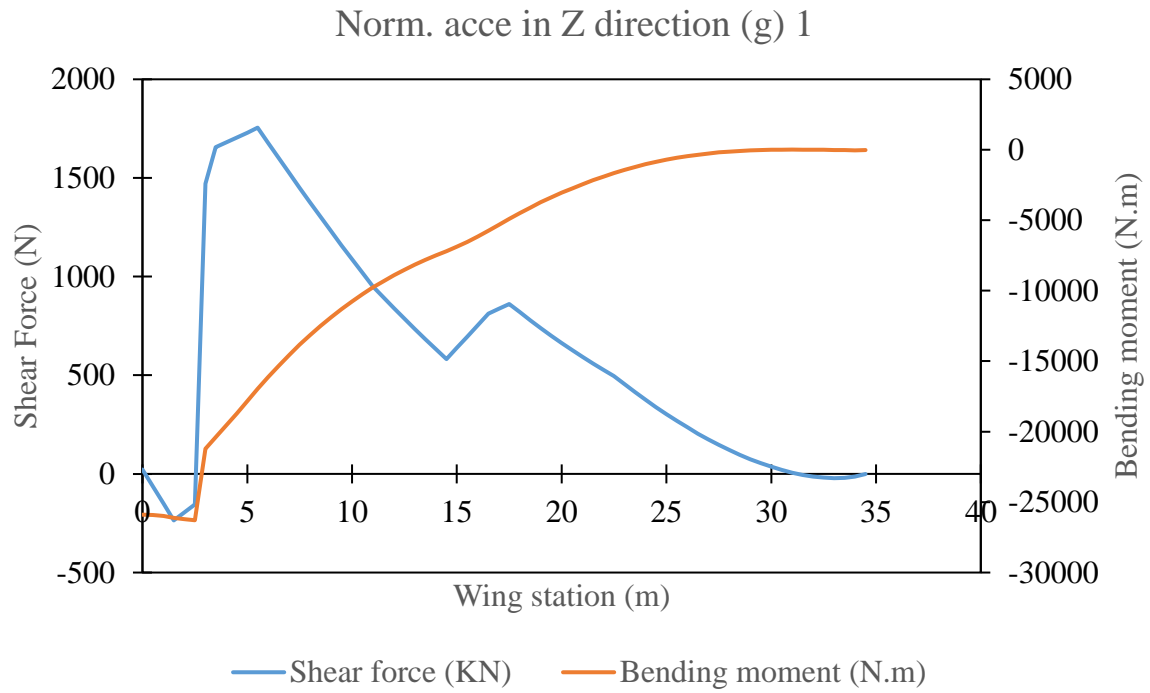


c)

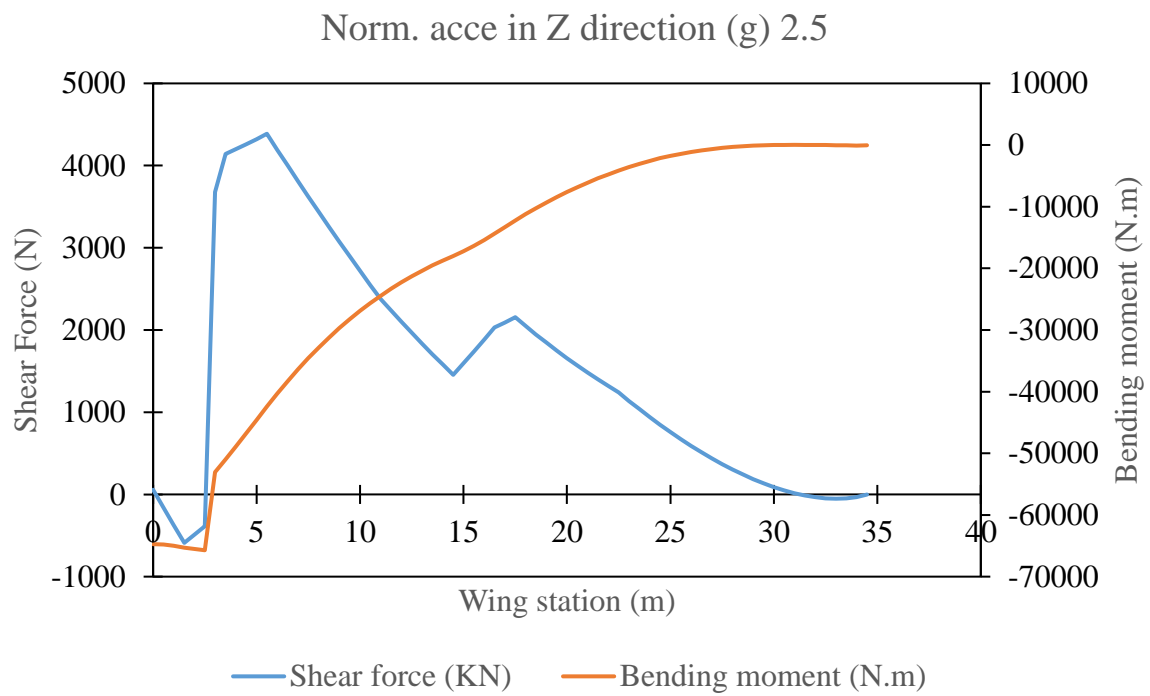


d)

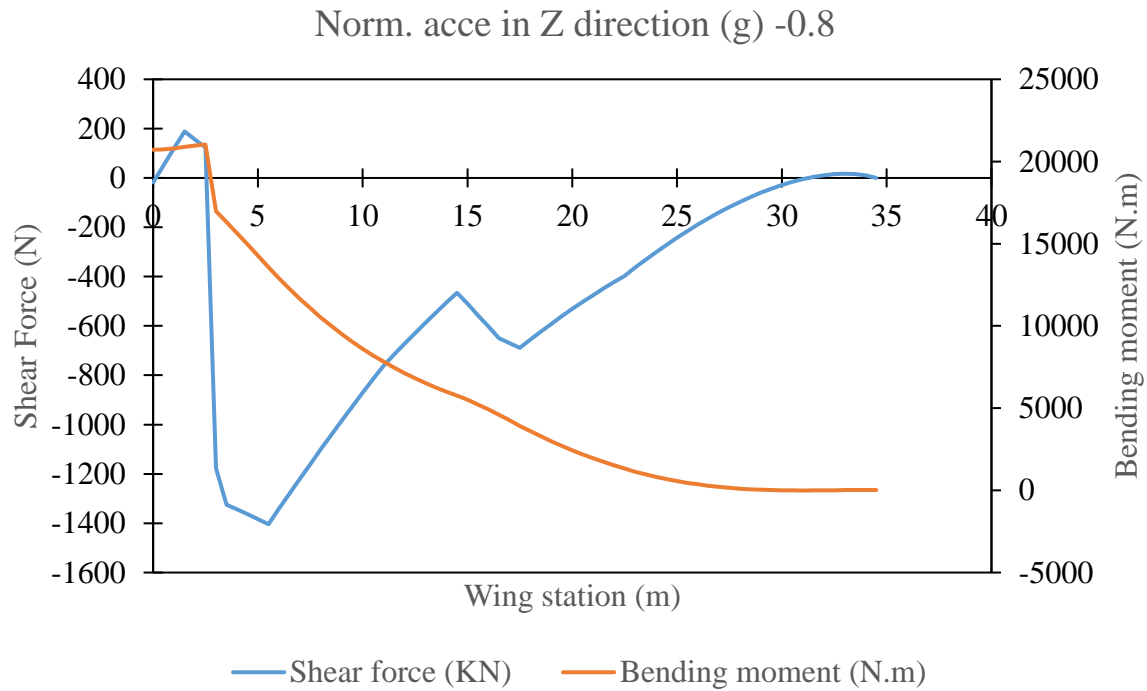
*Figure 4. Wing loading. a) Case 0, b) Case I, c) Case II, d) Case III*



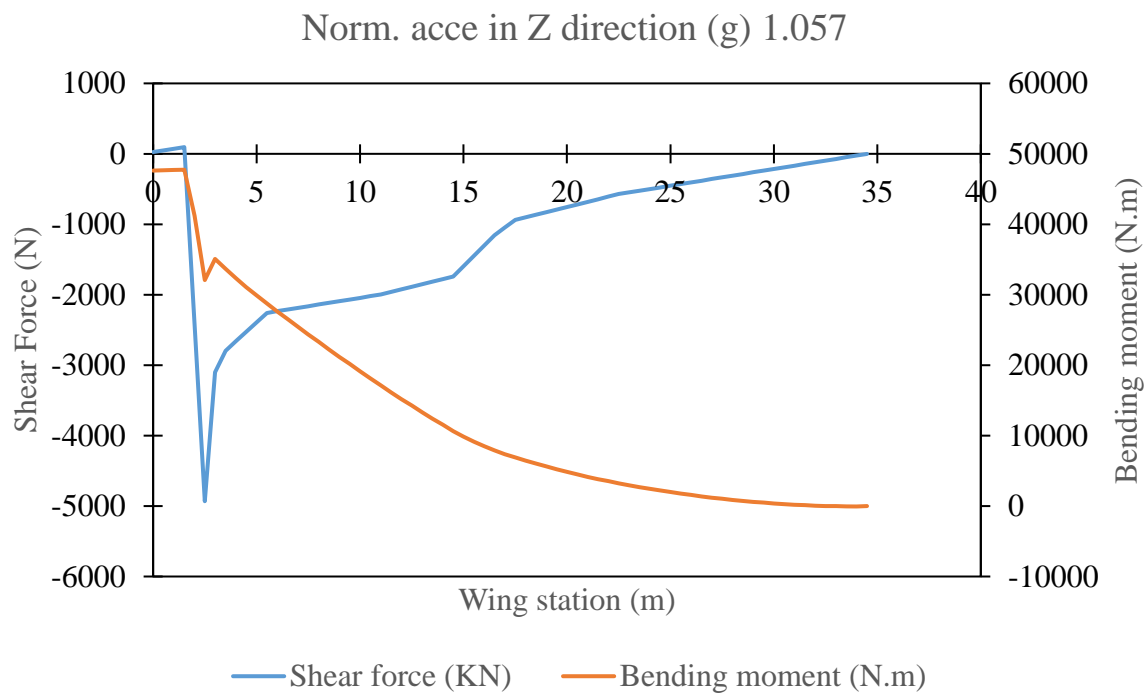
a)



b)



c)



d)

Figure 5. Shear Force and Bending moment diagram. a) Case 0, b) Case I, c) Case II, d) Case III

From the shear force and bending moment diagrams, it can be observed that for all loading conditions the bending moment is critical at the wing root section while the maximum shear force is achieved in the inboard nacelle. Both shear force and bending moment decrease

continuously along the span due to the inertial relief effect reaching minimum values at the wingtip. A sudden increase in the shear force and bending moment is encountered around the outboard nacelle due to the concentration of mass in this region.

From this analysis, it can be stated that the wing root section, inboard nacelle and outboard nacelle location are critical areas to be reinforced.

## 2. Wing Architecture

The proposed wing architecture is based on the Solar Impulse II a Swiss long-range experimental solar-powered aircraft intended to make the first circumnavigation of the Earth by a piloted fixed-wing aircraft using only solar power.

Characteristics	Si2	RMMA
Crew	1	2
Wingspan (m)	72	69.5
Weight (Tons)	2.3	2.7
Number of solar cells	17,248	
Number of propellers and batteries	4	4
Average airspeed (Km/h)	75	270
Atmosphere	Earth	Mars





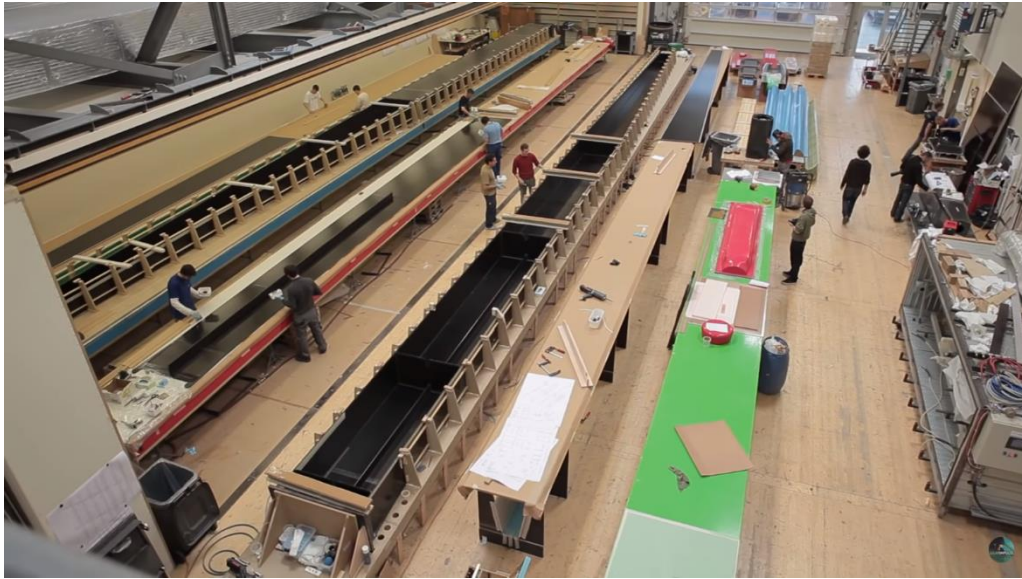


*Figure 6. Wing construction of the Solar Impulse 2 aircraft.*

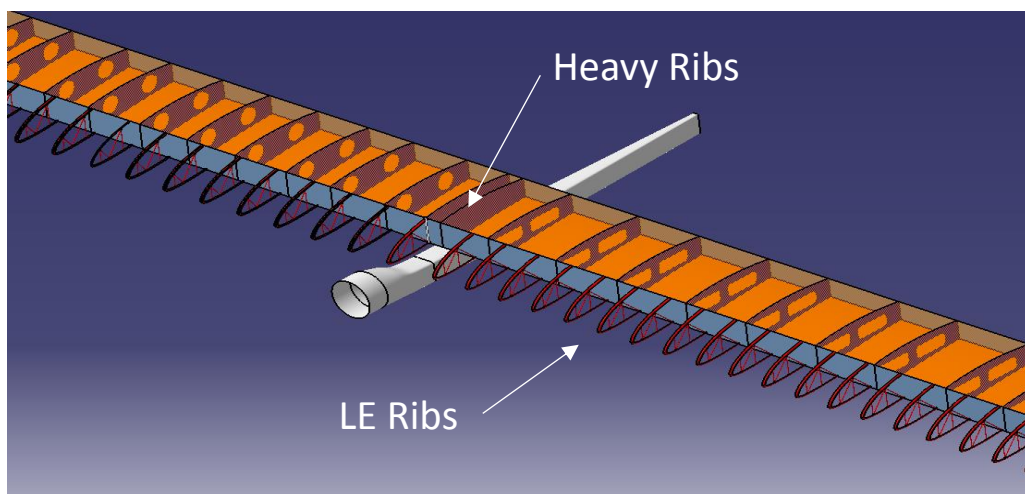
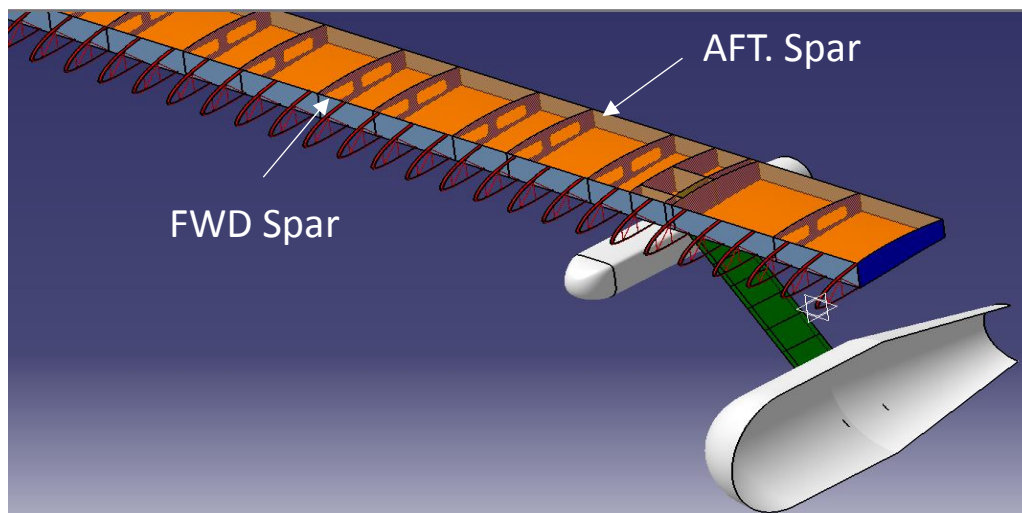
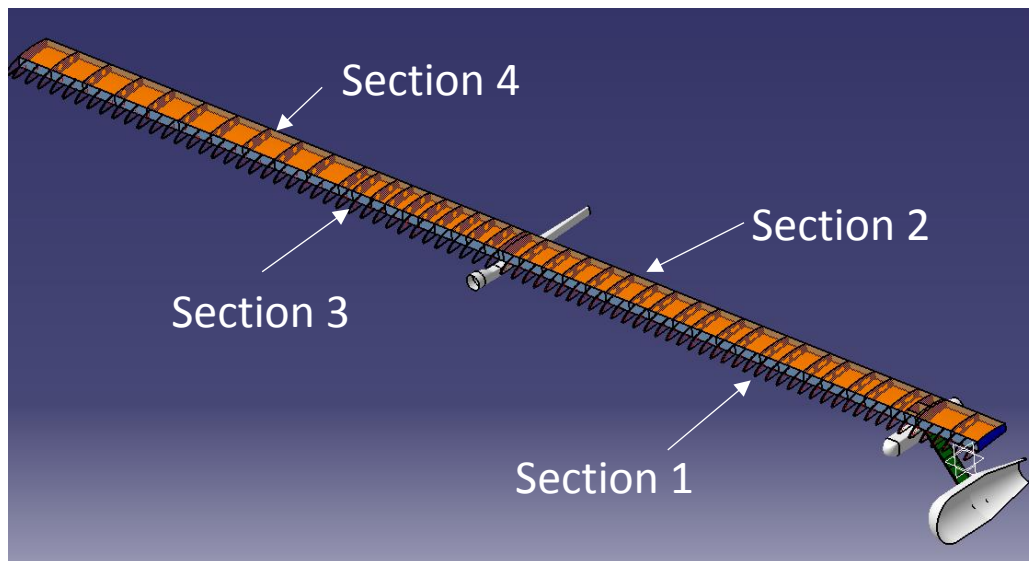
### **2.1. RMMA Wing's Architecture**

Due to the large wingspan, each half wing is separated into two sections (inboard and outboard). The wing is mainly supported by a central wing box structure with two spars located forward and afterward (FWD and AFT) at 20% and 60% of the chord respectively. 45 ribs are located along the span including two heavy ribs to reinforce the strut-wing attachment and two for the out nacelle. The distance between ribs is shorter in the inboard section to prevent structural instability in this heavily loaded region. The strut is made from a single cell box that transfer bending and torsion loading from the passenger's compartment into the wing's heavy ribs.

All structural components are made with composite sandwich construction with stacking sequence and material that vary depending on the structural component and the loading



requirements. The table below shows a summary of the configuration for each major structural component.



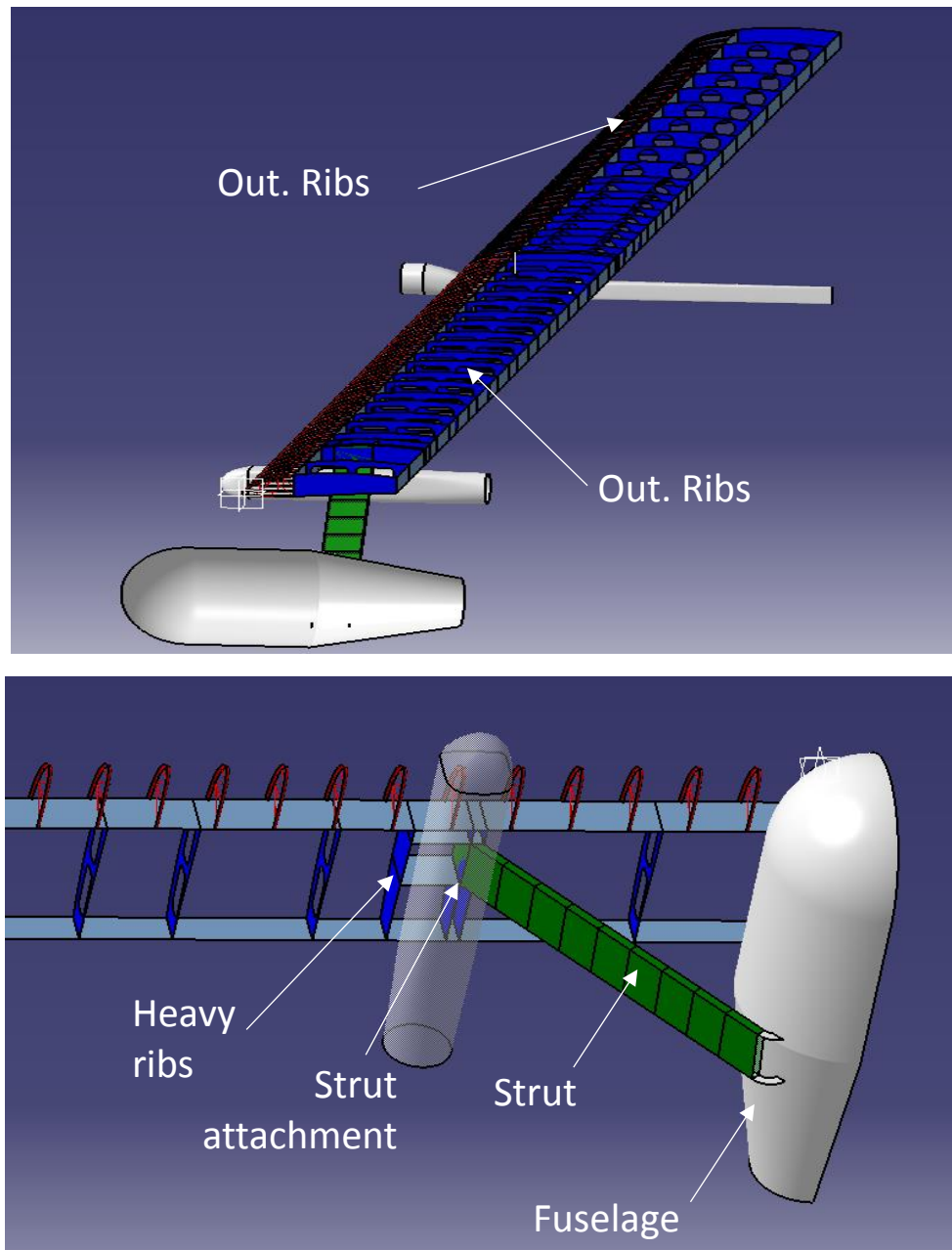


*Figure 7. RMMA wing's architecture*

COMPONENT	PART	TYPE	LAY-UP	FACESHEET		CORE		t (mm)	t <sub>total</sub> (mm)	Mass (Kg)
				MATERIAL	MATERIAL	MATERIAL	MATERIAL			
SPARS	Sec 1 (FWD & AFT)	Sandwich	[45,-45,60,30,0,90,0]/core/sym	8552s/AS4 3K (Woven)	HP60	8552s/AS4 3K (Woven)	HP60	10	11.8	66.2
	Sec 2 (FWD & AFT)	Sandwich	[45,-45,60,30,0,90,0]/core/sym	8552s/AS4 3K (Woven)	HP60	8552s/AS4 3K (Woven)	HP60	10	11.8	
	Sec 3 (FWD & AFT)	Sandwich	[45,-45,60,30,0,90,0]/core/sym	8552s/AS4 3K (Woven)	HP60	8552s/AS4 3K (Woven)	HP60	5	6.8	
	Sec 4 (FWD & AFT)	Sandwich	[45,-45,60,30,0,90,0]/core/sym	8552s/AS4 3K (Woven)	HP60	8552s/AS4 3K (Woven)	HP60	5	6.8	
WING SKIN	Sec 1 (Top & Bottom)	Sandwich	[0_3, 45,-45,0_2,60,30]/core/sym	8552/HM63 12K (UD)	HP100	8552/HM63 12K (UD)	HP100	10	12.4	282.2
	Sec 2 (Top & Bottom)	Sandwich	[0_3, 45,-45,60,30]/core/sym	8552/HM63 12K (UD)	HP100	8552/HM63 12K (UD)	HP60	10	11.8	
	Sec 3 (Top & Bottom)	Sandwich	[0_3, 45,-45,60,30]/core/sym	8552/HM63 12K (UD)	HP60	8552/HM63 12K (UD)	HP60	5	6.8	
	Sec 4 (Top & Bottom)	Sandwich	[0_2, 45,-45,60,30]/core/sym	8552/HM63 12K (UD)	HP60	8552/HM63 12K (UD)	HP60	5	6.6	
RIBS	Ribs (all)	Sandwich	[0,45]/core/[-45,90]	8552s/AS4 3K (Woven)	HP60	8552s/AS4 3K (Woven)	HP60	5	5.8	20.7
	Bulkhead ribs (all)	Sandwich	[0,45,90,-45]/core/[0,45,90,-45]	8552s/AS4 3K (Woven)	HP60	8552s/AS4 3K (Woven)	HP60	5	6.6	
STRUT	Spars (FWD & AFT)	Sandwich	[0_2,45,-45,60,30,0_2]/core/sym	8552s/IM7 12K (UD)	HP100	8552s/IM7 12K (UD)	HP100	5	7.1	12.2
	Skin (Top & Bottom)	Sandwich	[0_2,45,-45,60,30,0_2]/core/sym	8552s/IM7 12K (UD)	HP100	8552s/IM7 12K (UD)	HP100	10	12.1	
	Ribs (all)	Laminate	[0,45,-45,90]	8552s/AS4 3K (UD)		8552s/AS4 3K (UD)			0.8	
<b>TOTAL</b>									<b>(Kg)</b>	<b>381.3</b>

## 2.2. Materials

Due to its high specific strength and stiffness, Carbon Fiber Reinforced Plastics (CFRP) were chosen as the main structural material for the wing-box structure. Five different pre-preg variations of this material were considered in the design phase including plain wave and unidirectional tape with different filament type (high modulus and high strength). All the analysed materials are widely used for aerospace applications.

Due to the challenging bending stiffness required for the wing-box structure, a high modulus fibre was chosen for the skin panels and the wing's spars. The material selected was a unidirectional tape of HexTow HM63 (12K) with 8552 toughen epoxy resin manufactured by Hexcel.

Skin and web panels are stiffened using sandwich construction. Diab Divinycell PVC foam is used as a core material due to its low weight and relative high strength and stiffness. Two different core densities are used HP60 and HP100 depending on the strength requirements of a particular structural component.

The material properties were extracted directly from the manufacturer's website. In the case of all CFRP composites refer to [4] while for the core materials [5].

Hexcel 8552S AS4 3K plain weave		Hexcel 8552S AS4 3K unidirectional		Hexcel 8552 IM7 3K unidirectional		Hexcel 8552 HM63 12K unidirectional		Hexcel 8552 IM7 3K unidirectional		Diab Divinycell HP60		Diab Divinycell HP100	
T (C)	21	T (C)	21	T (C)	21	T (C)	21	T (C)	-54	T (C)	23	T (C)	23
Property	g/cc	Property	g/cc	Property	g/cc	Property	g/cc	Property	g/cc	Property	g/cc	Property	g/cc
$\rho$	1.57	$\rho$	1.57	$\rho$	1.58	P	1.58	$\rho$	1.58	$\rho$	0.065	$\rho$	0.1
Thickness	mm	Thickness	mm	Thickness	mm	Thickness	mm	Thickness	mm	Thickness	mm	Thickness	mm
t	0.195	t	0.130	t	0.131	T	0.195	t	0.131				
<b>ELASTIC PROPERTIES (in plane)</b>		<b>ELASTIC PROPERTIES (in plane)</b>		<b>ELASTIC PROPERTIES (in plane)</b>		<b>ELASTIC PROPERTIES (in plane)</b>		<b>ELASTIC PROPERTIES (in plane)</b>		<b>ELASTIC PROPERTIES</b>		<b>ELASTIC PROPERTIES</b>	
Property	MPa	Property	MPa	Property	MPa	Property	MPa	Property	MPa	Property	MPa	Property	MPa
E_1	64742	E_1	123589	E_1	151512	E_1	231319	E_1	147755	E_t	75	E_t	130
E_2	64363	E_2	138550	E_2	9308	E_2	9067	E_2	10308	E_c	80	E_c	135
G_12	4964	G_12	4826	G_12	4688	G_12	5929	G_12	5929	G	20	G	35
v12	0.046	v12	0.3185	v12	0.336	v12	0.316	v12	0.316	v	0.33	v	0.33
v21 c	0.054	v21 c	0.029	v21 c	0.024	v21 c	0.028	v21 c	0.028				
<b>STRENGTH PROPERTIES</b>		<b>STRENGTH PROPERTIES</b>		<b>STRENGTH PROPERTIES</b>		<b>STRENGTH PROPERTIES</b>		<b>STRENGTH PROPERTIES</b>		<b>STRENGTH PROPERTIES</b>		<b>STRENGTH PROPERTIES</b>	
Property	MPa	Property	MPa	Property	MPa	Property	MPa	Property	MPa	Property	MPa	Property	MPa
F_1 tu	769	F_1 tu	1928	F_1 tu	2206	F_1 tu	2489	F_1 tu	2434	F_t	1.8	F_t	3.5
F_1 cu	844	F_1 cu	1484	F_1 cu	1731	F_1 cu	1351	F_1 cu	2013	F_c	0.95	F_c	2.0
F_2 tu	753	F_2 tu	64	F_2 tu	64	F_2 tu	45	F_2 tu	66	F_s	0.85	F_s	1.6
F_2 cu	781	F_2 cu	268	F_2 cu	286	F_2 cu	381	F_2 cu	381				
F_12	56	F_12	92	F_12	91	F_12	100	F_12	78				

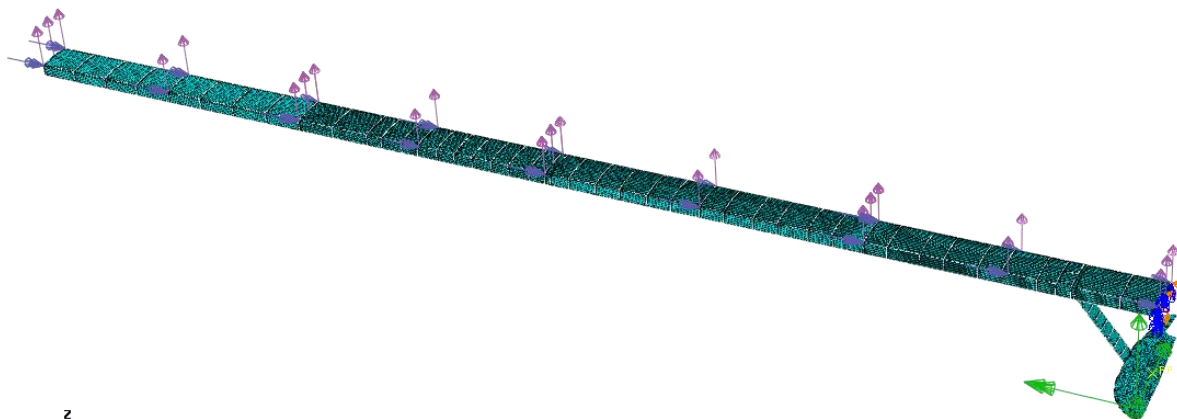
### 3. Structural analysis

A static FEA model in Abaqus V.6.14 [6], is carried out to obtain the stress and strain distribution of the proposed wing-box architecture and determine if the structure satisfies the overall strength and stiffness requirements for each of the analysed loading conditions. Linear perturbation buckling analysis is carried out to verify that there is not structural instability that could compromise the integrity of the structure.

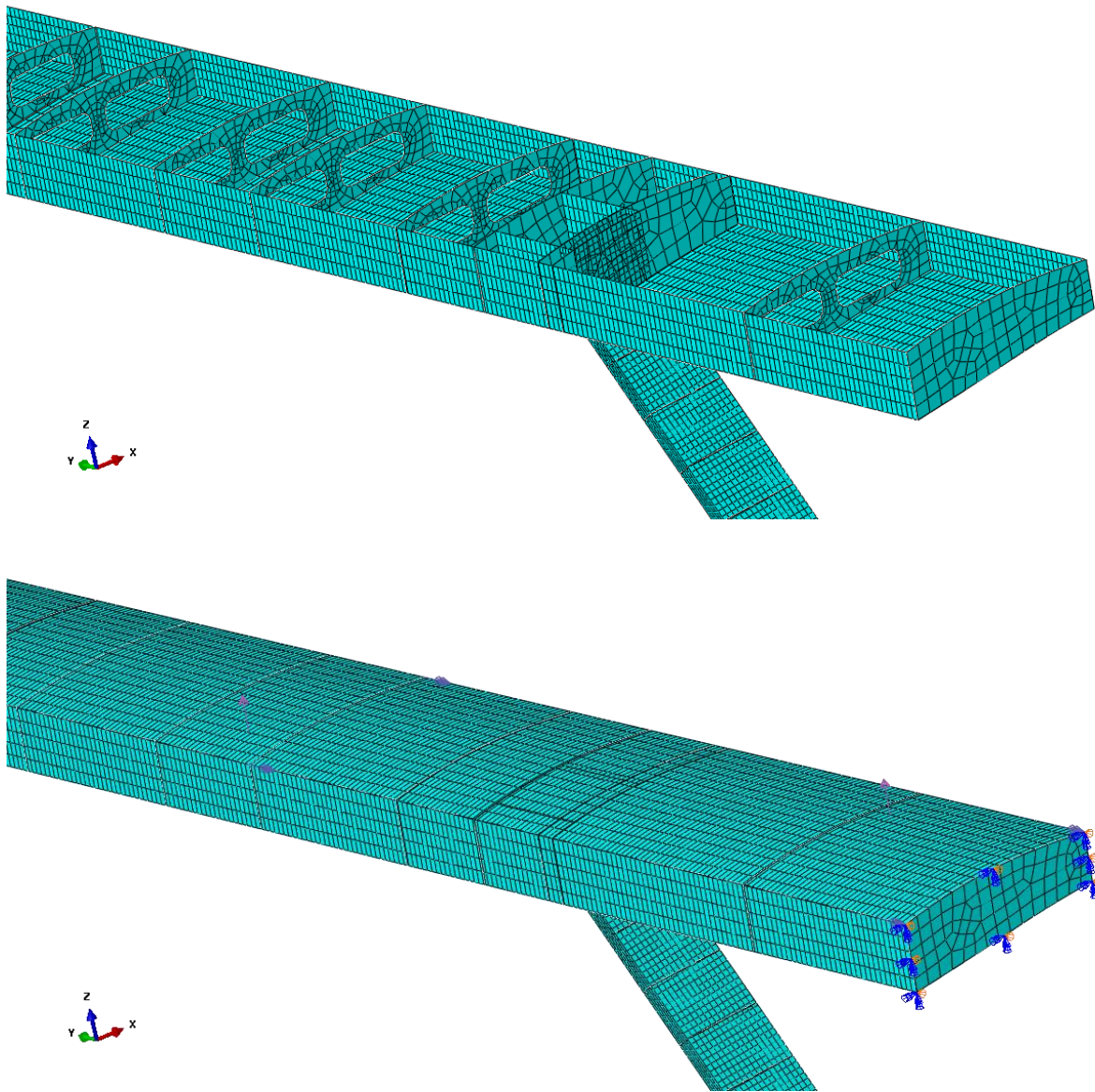
The FEA model is based on a simplified surface CAD model of half of the structure developed in Catia V5 and imported in Abaqus for pre-processing. The whole structure is modelled with deformable 2D shell elements with reduced integration. The average mesh size is 30mm for 45617 elements in total. All the wing-box independent components were connected using a tie constraint.

Composite laminates are modelled with an elastic lamina where Young's modulus, shear modulus and Poisson ratio parallel and perpendicular to the fibre ( $E_1$ ,  $E_2$ ,  $G_{12}$ ,  $\nu_{12}$ ) were obtained directly from the manufacturer's datasheet and qualification data report and summarized in the table above. Additionally, the longitudinal and transverse ultimate strength ( $F_{1tu}$ ,  $F_{1cu}$ ,  $F_{2tu}$ ,  $F_{2cu}$ ) were also included in order to estimate first ply failure. For simplicity, the core material was assumed isotropic and elastic with perfect plasticity (stress remains constant after plasticity). To be conservative the yield strength in compression was taken as the material yield strength.

The weight distribution along the span is introduced through non-structural masses at different rib locations. The lift force is applied at each of the four wing sections as surface traction in the skin top surface. Inertial relief is activated as a boundary condition to account for the translational acceleration required to achieve static equilibrium. Displacements and rotations ( $U_2$ ,  $UR_1$ ,  $UR_3$ ) are restrained in the root due to symmetry around the mid-plane axis.



a)



b)

*Figure 8. FEA model, a) Mesh and loading, b) Mesh detail inboard section*

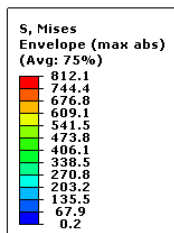
#### 4. Result.

Results obtained from the FEA model were used in an iterative process that allowed the optimization of lay-up in the main wing panels by reducing the structural weight while maintaining the wing's integrity.

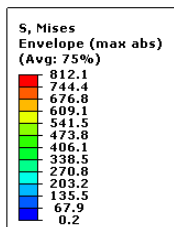
This section shows an example of the results from the FEA analysis for loading Case I (n=2.5). The results for the remaining loading cases are summarized in Table 3.

The maximum Von Mises stress across the thickness (envelope) is plotted to visualize the variation of the stress intensity in the wing-box structure (spars, ribs, strut skin) and spot region of heavy stress concentration. It can be observed that the stress level varies along the span reaching maximum values at the wing box root and in the strut attachment. The highest stress concentrations are found to occur in the vicinity of the strut attachment (in the bottom skin) and in the mid-plane of the wing root. It is also observed that spars and ribs located near the inboard nacelle are highly stressed due to the presence of the strut attachment that transfers the inertial loads from the fuselage. Additionally, this section also resists the inertial relief of the motors, batteries, rockets and their components.

In the rest of the structure, the stress distribution seems to follow a smooth decrease along the span with maximum stress values lower than 200 MPa in the majority of the structure.

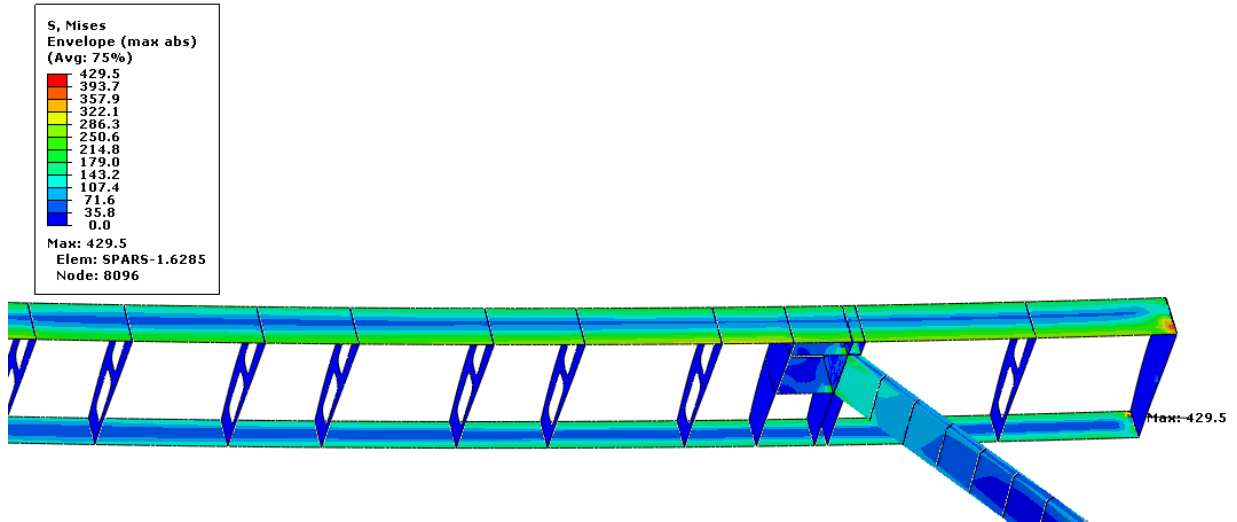


a)

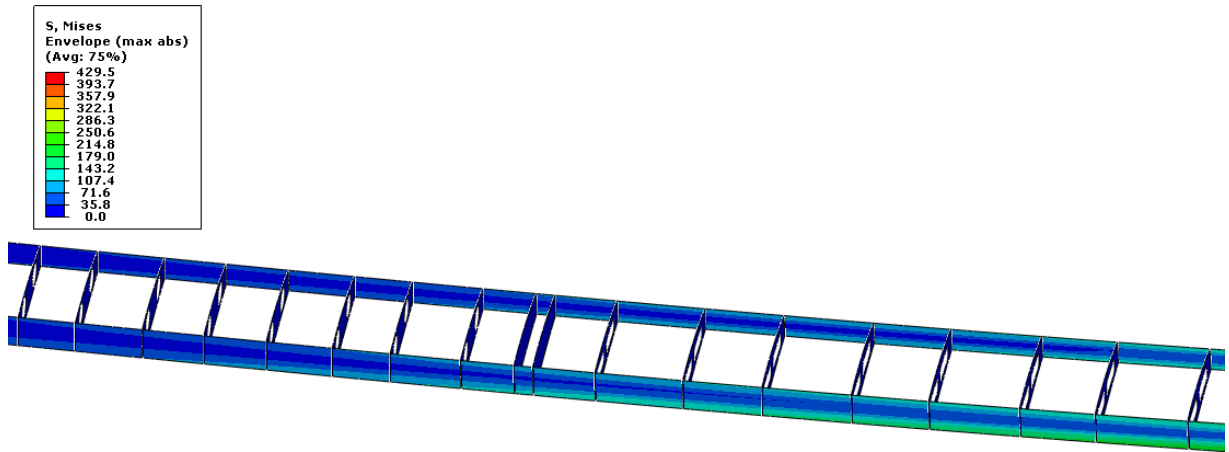


b)

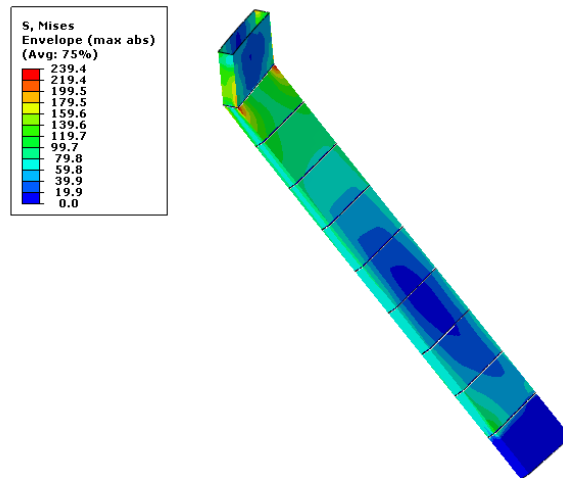




c)



d)



e)

Figure 9. Max. Absolute Mises stress distribution for Case I [MPa]. a) top skin, b) bottom skin, c) spars-ribs inb, d) spars-ribs out, e) strut

The integrity of the sandwich face-sheets is assessed using Hashin's damage initiation criteria for each ply. This criterion includes four different failure modes (fibre rupture in tension, fibre buckling and kinking in compression, matrix cracking under transverse tension and shearing, and matrix crushing under transverse compression and shearing). Damage initiation refers to the onset of degradation at a material point and is given by the following general forms [7]:

Tensile fibre mode:

$$F_f^t = \left(\frac{\sigma_{11}}{X^T}\right)^2 + \left(\frac{\sigma_{12}}{S^L}\right)^2 = 1$$

Fibre compressive mode:

$$F_f^c = \frac{\sigma_{11}}{X^C} = 1$$

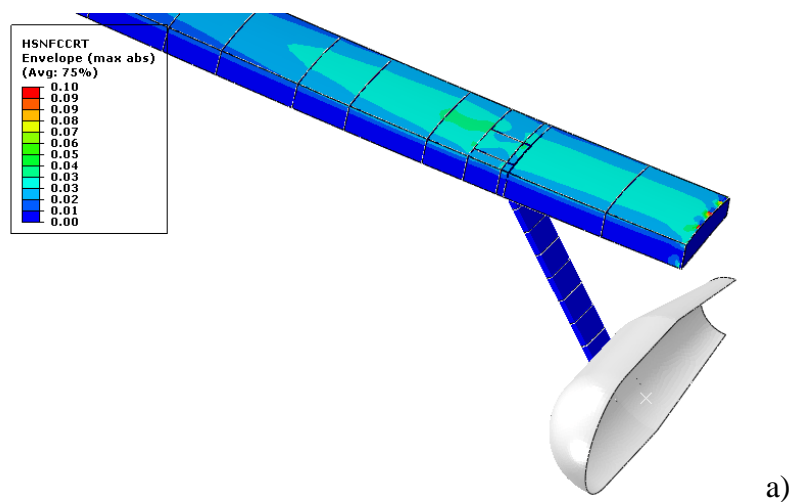
Tensile matrix mode:

$$F_m^t = \left(\frac{\sigma_{22}}{Y^T}\right)^2 + \left(\frac{\sigma_{12}}{S^L}\right)^2 = 1$$

Compressive matrix mode:

$$F_m^c = \left(\frac{\sigma_{22}}{2S^T}\right)^2 + \left[\left(\frac{Y^C}{2S^T}\right)^2 - 1\right] \left(\frac{\sigma_{22}}{Y^C}\right) + \left(\frac{\sigma_{12}}{S^L}\right)^2 = 1$$

Under this loading case, all Hashin's failure coefficients are well below 1 what indicates that all CFRP laminates in the structure have not failed. This is depicted in Figure 10 where the maximum Hashin's failure index (across the laminate) is lower than 1.



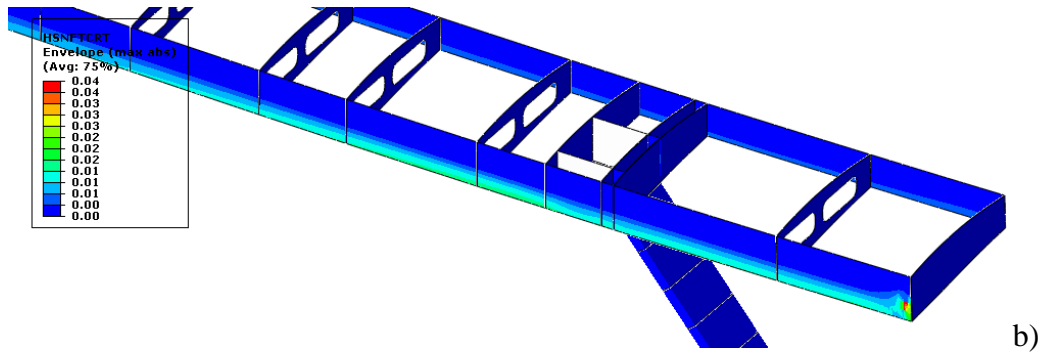


Figure 10. Hashin's failure criteria (fibre tension) for load case I ( $n=2.5$ ). a) inboard top skin, b) inboard main spars and ribs.

The integrity of the sandwich core was also analysed to ensure that no plastic deformation is observed. From the figure below, it can be observed that the maximum strain in the core section is 0.48% which is a value much lower than the plastic strain of the material. This observation can be corroborated by looking at the equivalent plastic strain, which for the current loading case is zero.

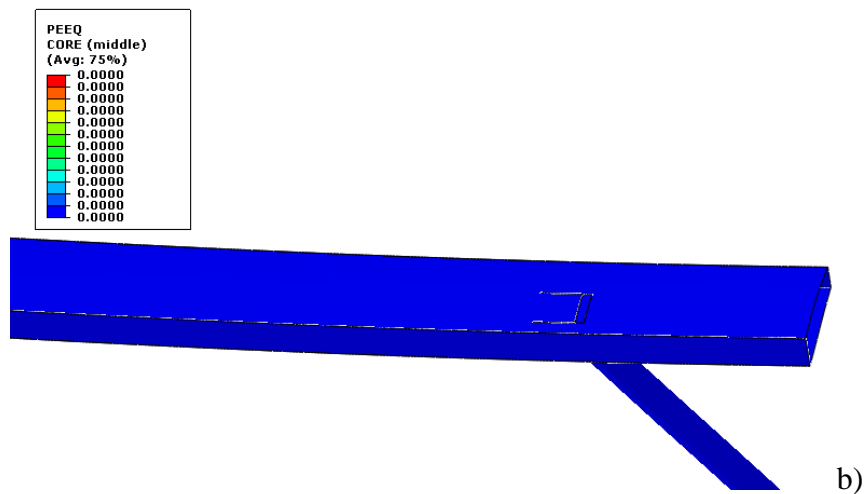
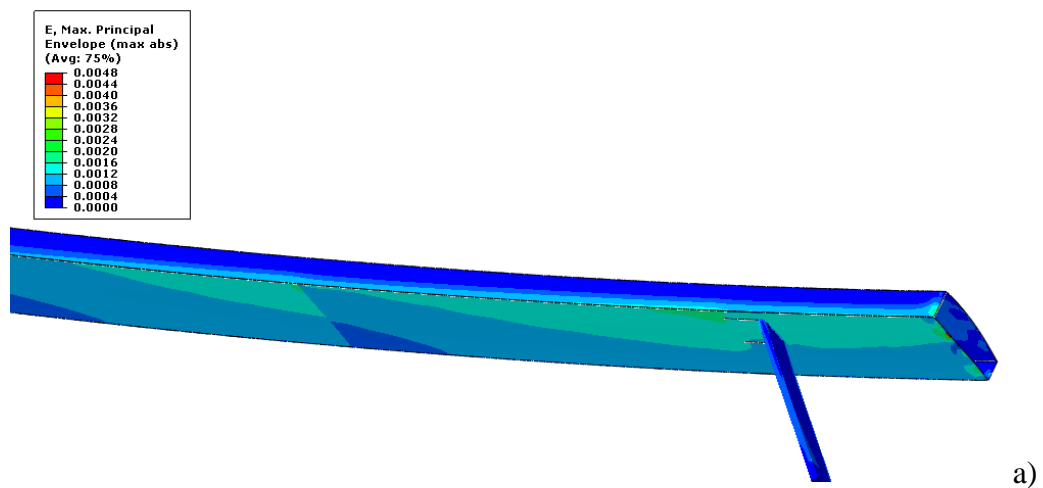


Figure 11. a) Core's maximum principal strain (skin, spar and strut), b) Core's plastic strain (skin, spar and strut)

Structural stability was also studied for the loading case. The following table shows the first five buckling modes of the structure. It is observed that structural instability is not present in this loading condition since all eigenvalues have a magnitude higher than one.

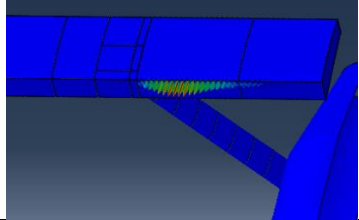
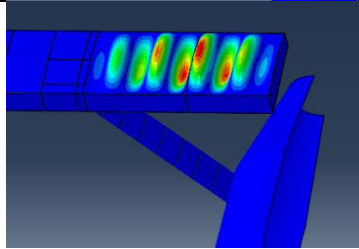
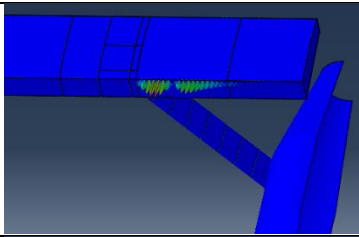
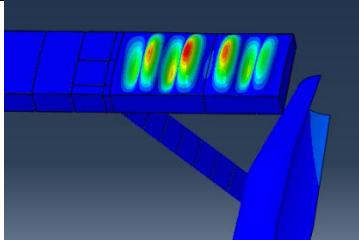
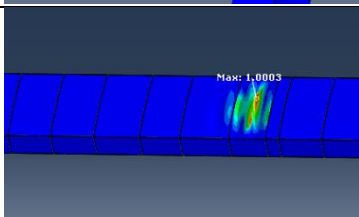
Mode	Eigenvalue ( $\lambda$ )	Mode-shape
1	1.0278	
2	1.0376	
3	1.0453	
4	1.0464	
5	1.0516	

Table 2. First five buckling modes (Case I)

The tip deflection for each analysed load case is shown below:

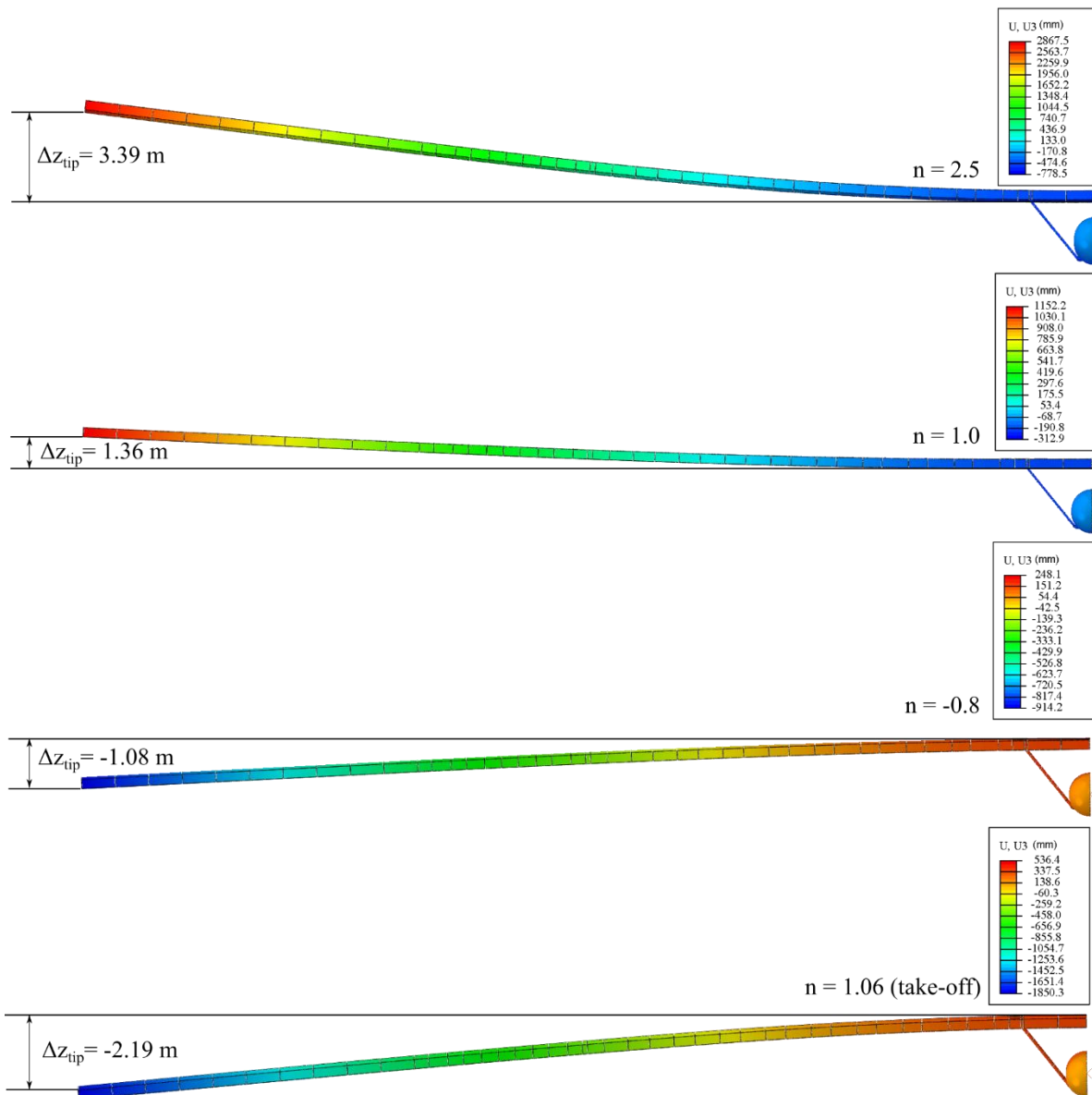


Figure 12. Wing deflection at different loading conditions.

$\Delta z_{tip}$  = absolute relative vertical displacement between the wingtip and the wing root

U3 = vertical displacement at any point from the base model reference frame.

Case	n (g)	Max. Hashin failure index	$\Delta z_{tip}$ (m)	$\sigma_{max}$ (Mpa)	$\lambda_1$	Failure?	Instability?	Comment
0	1	0.14	1.36	325.9	1.027	NO	NO	Steady level flight at Vs
I	2.5	0.86	3.39	812	8	NO	NO	(+) symmetric at Va
II	-0.8	0.037	-1.08	259.2	3.458	NO	NO	(-) symmetric at Va
III	1.06	0.19	-2.19	583.6	1.23	NO	NO	Steady take-off with rockets

Table 3. Summary of FEA analysis for different load cases

## CONCLUSIONS

A preliminary wing structure architecture is proposed to ensure that the wing-box can support limit loads without permanent deformation and that the deformation is maintained within the limits for safe operation. The wing is mainly supported by a central wing box structure with two spars (FWD and AFT) at 20% and 60% of the chord respectively and 45 ribs located along the span including two heavy ribs to reinforce the strut-wing attachment and two for the out nacelle. The distance between ribs is shorter in the inboard section in order to prevent structural instability in this heavily loaded region. The strut is made from a single cell box that transfer bending and torsion loading from the passenger's compartment into the wing's heavy ribs. All structural components are made with composite sandwich construction with stacking sequence and material that vary depending on the structural component and the loading requirements. Carbon Fiber Reinforced Plastics (CFRP) HexTow HM63/8552 is chosen as the main structural material due to its high specific stiffness. Divinycell foams (HP60 & HP100) are used as a core material due to their low weight and relative high strength and stiffness. The total weight of the aircraft's wing-box is 762 Kg that corresponds to 84% of the available weight for the wing structure.

A static FEA model and a linear perturbation buckling analysis is developed in Abaqus V.6.14 in order to verify that the proposed wing-box structure satisfies the strength requirements and determine if there is structural instability that could compromise the integrity of the structure. The structure is modelled with deformable 2D shell elements with reduced integration. The average mesh size is 30mm for 45617 elements in total. Composite laminates are modelled following the corresponding stacking sequence using three integration points per ply. All wing-box components are connected using a tie constraint. External loads (airloads and rockets trust) are placed in equilibrium with inertial forces using inertial relief boundary condition. For this, approximate weight distribution in the span-wise direction is introduced through non-structural masses at different rib locations. The lift distribution is assumed to be perfectly elliptical and approximated by four-step distributions along the span which are applied as surface traction in the skin top surface. Displacements and rotations (U2, UR1, UR3) are restrained in the root

due to symmetry around the mid-plane. Four loading conditions are considered: i) level flight at stall speed ( $n=1$ ), ii) symmetric (+) manoeuvre ( $n=2.5$ ), iii) symmetric (-) manoeuvre ( $n=-0.8$ ), iv) steady take-off at full rocket thrust ( $T=10675$  N).

It is observed that for all the analysed conditions, the proposed wing box structure complies with the strength requirements and no structural instability is present. It is also observed that the wing-tip deflection is particularly high and it could compromise the normal operation of flight control surfaces and massively modify the aerodynamic response of the airplane. For such reasons, it seems necessary to include the effect of the wing deformation in the aerodynamic analysis during the early design phases. It is also advised to perform aero-elastic analysis in order to verify that flutter instability is not present during the operational flight velocities range.

## REFERENCES

- [1] D. Raymer, J. French, F. Finger, A. Gómez, J. Singh, R. G. Pillai, M. Monjon, J. M. d. Souza and A. Levy, "The Raymer Manned Mars Airplane: A conceptual design and feasibility study," in *AIAA SciTech Forum*, 2021.
- [2] M. Drela, *Flight Vehicle Aerodynamics*, MIT press, 2014.
- [3] D. Howe, *Aircraft Loading and Structural Layout*, Weley, 2004.
- [4] Hexcel, "Data sheets," 12 2020. [Online]. Available: <https://www.hexcel.com/Resources/DataSheets/>. [Accessed 12 2020].
- [5] Diab, "Diab products," 12 2020. [Online]. Available: <https://diabgroup.com/products/divinycell-pvc/divinycell-hp/>. [Accessed 12 2020].
- [6] Dassault Systemes, *Abaqus Analysis User's guide*, 2020.
- [7] Z. Hashin, "Failure criteria for unidirectional fiber composites," *Journal of Applied Mechanics*, vol. 47, pp. 329-334, 1980.